


Article

Optimization of the Adsorption/Desorption Contribution from Metal-Organic-Heat-Carrier Nanoparticles in Waste Heat Recovery Applications: R245fa/MIL101 in Organic Rankine Cycles

Giovanna Cavazzini * and Serena Bari

Department of Industrial Engineering, University of Padova, Via Venezia 1, 35131 Padova, Italy; serena.bari@unipd.it

* Correspondence: giovanna.cavazzini@unipd.it

Abstract: The efficient recovery of low temperature waste heat, representing from 25% up to 55% of the energy losses in industrial processes, still remains a challenge and even Organic Rankine Cycles (ORCs) experience a strong efficiency decay in such a low temperature operating range ($T < 150$ °C). In similar heat transfer processes, several nanofluids have been proposed as a solution for increasing heat transfer efficiency, but they produced only moderate enhancements of the heat transfer efficiency in comparison with pure fluids. This paper aims at numerically assessing the potential gain in efficiency deriving from the application of an unconventional type of nanoparticles, the metal-organic heat carriers (MOHCs), in the ORC field. In comparison with standard nanoparticles, these MOHCs make it possible to extract additional heat from the endothermic enthalpy of desorption, with a theoretically high potential for boosting the heat transfer capacity of ORC systems. In this paper a numerical model was developed and customized for considering the adsorption/desorption processes of the pure fluid R245fa (pentafluoropropane) combined with a crystal structure for porous chromium terephthalate (MIL101). The R245fa/MIL101 nanofluid behavior was experimentally characterized, defining proper semi-empirical correlations. Then, an optimization procedure was developed, combining the numerical model with a PSO algorithm, to optimize the thermodynamic conditions in the ORC so as to maximize the contribution of desorption/adsorption processes. The results confirm the increase in net power output (+2.9% for 100 °C) and in expander efficiency (+2.4% for 100 °C) at very low heat source temperature. The relevance of tuning the operating cycle and the nanofluid properties is also demonstrated.



Citation: Cavazzini, G.; Bari, S. Optimization of the Adsorption/Desorption Contribution from Metal-Organic-Heat-Carrier Nanoparticles in Waste Heat Recovery Applications: R245fa/MIL101 in Organic Rankine Cycles. *Energies* **2022**, *15*, 1138. <https://doi.org/10.3390/en15031138>

Academic Editors:
Annunziata D'Orazio and
Arash Karimipour

Received: 14 January 2022
Accepted: 2 February 2022
Published: 3 February 2022

Publisher's Note: MDPI stays neutral with regard to jurisdictional claims in published maps and institutional affiliations.



Copyright: © 2022 by the authors. Licensee MDPI, Basel, Switzerland. This article is an open access article distributed under the terms and conditions of the Creative Commons Attribution (CC BY) license (<https://creativecommons.org/licenses/by/4.0/>).

Keywords: metal-organic heat carriers; adsorption; waste heat; ORC; two-phase fluid

1. Introduction

One of the pillars of the energy transition of the industrial sector is certainly to make industrial processes more circular and more energy efficient. However, nowadays, the process efficiency in this sector is still too low [1,2] and a non-negligible share of the energy losses is represented by low temperature heat, wasted due to the lack of internal heat demand [3].

Even if there are promising technologies for recovering waste heat (such as organic Rankine cycles, ORC) [4,5], their effective and sustainable application is still a challenge due to the strong efficiency decay for low-grade waste heat ($T < 150$ °C). In particular, as regards ORC, the few available modules in the market have low efficiencies (between 5% and 9%) and high costs (5000 to 8000 €/kW [6–8]) with negative consequences in terms of sustainability and profitability.

One of the main reasons for these poor efficiency values is the strong performance decay experienced by pure organic fluids in the case of heat sources characterized by temperatures lower than 150 °C and especially around 100 °C [9].

Several studies have been carried out to identify a working fluid with characteristics suitable for low grade heat sources. Screening criteria based on the fluid thermodynamic and chemical properties [10–13], the Jakob number [14] and on tuning the heat source temperature and the working fluid critical temperature [15–17] have all been proposed. However, it is plain to see that the best working fluid is still far from being identified.

In similar heat transfer processes, nanofluids [18] have been proposed as a solution for increasing heat transfer efficiency [19–24]. The most significant literature deals with nanofluids applied in solar technologies [25–30]. Experimental and numerical approaches were adopted to analyse the performance of different types of nanoparticles (i.e., Al_2O_3 , Al, SiO_2 , CuO, Au, Fe_2O_3 , . . .) [31–35], also considering their possible combination (i.e., $\text{Al}_2\text{O}_3/\text{TiO}_2$) [36,37]. However, besides the technical challenges (stability, deposition, maintenance, etc.) faced for their use, the nanofluid performance in these applications showed a decay at low temperatures resulting in moderate enhancements of the heat transfer efficiency in comparison with pure fluids [25,36].

To overcome this issue, molecular engineers have studied how to increase the amount of heat extracted from the heat source and concluded that the contribution of the nanoparticles in terms of sensible heat is too limited at low temperature to have a positive impact on the recovery efficiency, so to increase the performance at these temperature values, they developed an innovative type of nanoparticles, the so-called metal-organic heat carriers (MOHCs), whose structure presents porosity, engineered on purpose to allow the molecule to absorb and desorb the pure fluid in which it is suspended depending on temperature and pressure values [38]. Since the desorption process is endothermic, it allows to extract an additional amount of heat from the heat source with a potential significant increase of the recovery efficiency of the nanofluid in comparison with the pure fluid.

The assessment of the potential increase in ORC performance deriving from the use of these MOHC-based nanofluids in low-grade heat recovery applications started with some preliminary analyses carried out on the pure fluid R245fa (pentafluoropropane) paired with nanoparticles of the MOHC family termed MIL101 [39], a crystal structure for porous chromium terephthalate whose characteristics are suitable for adsorption/desorption processes [40]. In these studies, semi-empirical correlations were determined in order to model the reversible adsorption/desorption process of the MIL101 in the R245fa [41,42]. These correlations were included in the numerical model of an ORC in order to estimate the impact of the adsorption/desorption process on the system performance. The results highlighted a promising potential of the MOHC nanoparticles in terms of area reduction in the heat exchanger but not significantly in terms of net power output. This limited performance improvement achieved by the R245fa/MIL101 nanofluid was due to the non-optimal mass fraction and the non-optimal thermodynamic conditions preventing from the maximization of the adsorption/desorption processes.

The primary aim of this paper is to move on from the results in [41,42], overcoming the limits of the non-optimal operating conditions and maximizing the ORC efficiency gain by optimally tuning the desorption process for the MIL101/R245fa nanofluid and the cycle parameters (pressure and temperature above all). This goal required the development of a new numerical model allowing to include the nanofluid behavior and in particular the desorption/adsorption processes within the optimization procedure of the ORC cycle parameters.

Moreover, to address future research in nanofluids applied to energy conversion processes, the paper also investigates possible paths for molecular improvements of the MIL101 characteristics. In particular, the paper analyses the benefits deriving from a theoretical increase in MIL101 uptake capacity.

The paper is organized as follows: Section 2 presents the numerical model of ORC developed for pure fluids, whereas Section 3 enters the details of the nanofluid characterization and behaviour, explaining the main equations adopted for developing the numerical model. In Section 4 the enhancements achieved by the use of the nanofluid in ORC are

critically discussed and a potential path for the MOHC molecule performance enhancement is investigated.

2. Numerical Model of ORC for Pure Fluids

The ORC system was investigated in a simple and sub-critical configuration, without any regeneration process, since it was widely demonstrated both in literature and by the market that this is the most effective configuration for low grade heat recovery applications (Figures 1 and 2) [43,44].

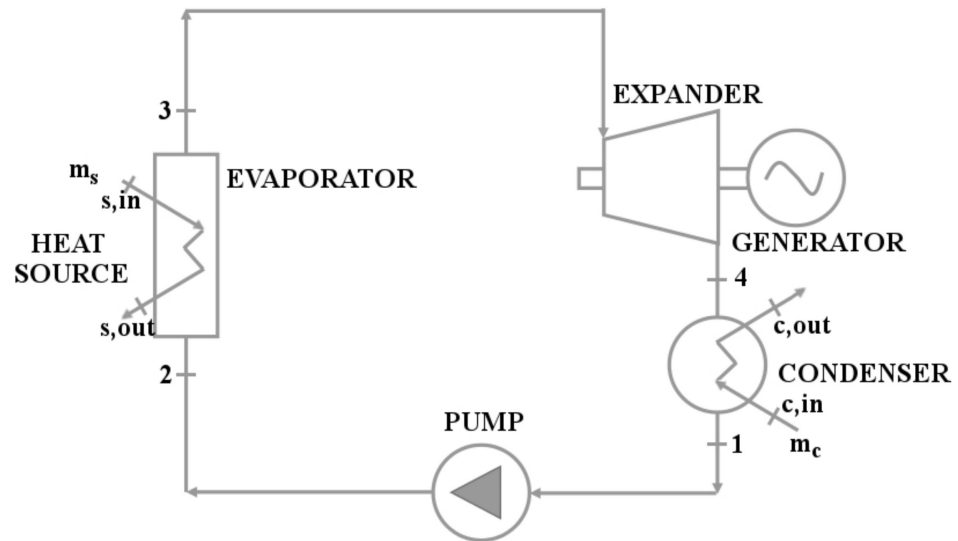


Figure 1. Scheme of the investigated ORC configuration.

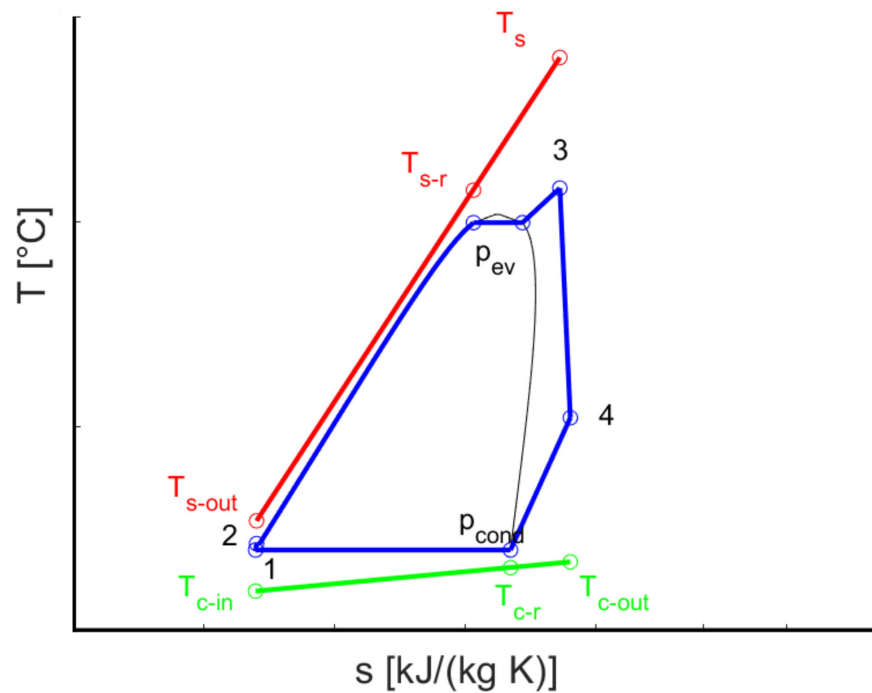


Figure 2. ORC cycle in a T-s diagram.

The low grade heat source was assumed to be a mass flow rate m_s of water equal to 5 kg/s at the temperature $T_{s,in}$ of 100 $^{\circ}\text{C}$, whereas for the cold source in the condenser, water at the temperature $T_{c,in}$ of 10 $^{\circ}\text{C}$ was fixed [9,45].

As regards the numerical model, the following assumptions were made:

- the pump isentropic efficiency:

$$\eta_{is, pump} = \frac{h_{2is} - h_1}{h_2 - h_1} \quad (1)$$

was assumed equal to 0.8 [46].

- The expander efficiency

$$\eta_{exp} = \frac{h_3 - h_4}{h_3 - h_{4is}} \quad (2)$$

was set equal to 0.8 for the pure fluid R245fa [47]. In the nanofluid case, as it will be better explained later on, the expander efficiency was determined within the optimization procedure since it resulted to be positively affected by the adsorption process of the R245fa molecule into the MIL101 porous structure [38]. More details can be found in Section 3.4.

- As regards the vapour quality at the end of the expansion process, the lower limit was fixed equal to 0.85 in order to avoid damages in the expander due to the excessive presence of liquid droplets [48].
- Pressure drops and heat losses were not considered [49].

To evaluate the cycle performance, the efficiency η_{syst} of the ORC system was determined, considering both the thermal efficiency η_{th} and the heat recovery efficiency χ :

$$\eta_{syst} = \frac{P_{net}}{Q_s} = \frac{P_{net}}{Q_{evap}} \cdot \frac{Q_{evap}}{Q_s} = \eta_{th} \chi \quad (3)$$

where P_{net} is the net power output P_{net} over the thermal power absorbed in the evaporator Q_{evap} and Q_s is the heat flux which could be transferred to the working fluid if the heat source was cooled to the ambient temperature ($T_0 = 20^\circ\text{C}$).

The model was developed in Matlab environment, whereas CoolProp was used for the thermodynamic data of the pure fluid R245fa [50]. More details about the equations can be found in [41,42].

3. Numerical ORC Model for the R245fa-MIL101 Nanofluid

Unlike pure organic fluids and conventional fluid mixtures, the properties of a nanofluid cannot be obtained by standard commercial software like CoolProp and hence to numerically investigate its behavior is necessary to determine proper correlations modelling the characteristics as a function of pressure and temperature values.

3.1. Experimental Determination of Adsorption Characteristics of the Nanofluid R245fa-MIL101

As explained in the introduction section, the potential of MOHC particle is related to the possibility of extracting/releasing additional heat from the heat source and to the cold source as a consequence of the adsorbing/desorbing process in their porous structure [38]. Since the uptake capacity of the porous structure depends not only on the operating conditions (pressure and temperature values) but also on the pure fluid characteristics and on its matching with the structure of the adopted MOHC [51], the adsorption/desorption process has to be experimentally investigated in order to numerically model it, so in previous studies, the MIL101 [52] was selected as a MOHC nanoparticle and its behaviour in combination with the pure fluid R245fa was experimentally analysed, as summarized in the following sub-sections [41,42].

3.1.1. Identification of the Theoretical Model of the R245fa-MIL101 Nanofluid

In literature, the adsorption behaviour of MOHC-based nanofluids can be traced to a few theoretical models, the most representative of which are summarized in Figure 3 [51]. As it can be seen in this figure, each behaviour is characterized by a different shape of

the isotherm, describing the amount of gas adsorbed in the molecule as a function of its pressure at constant temperature.

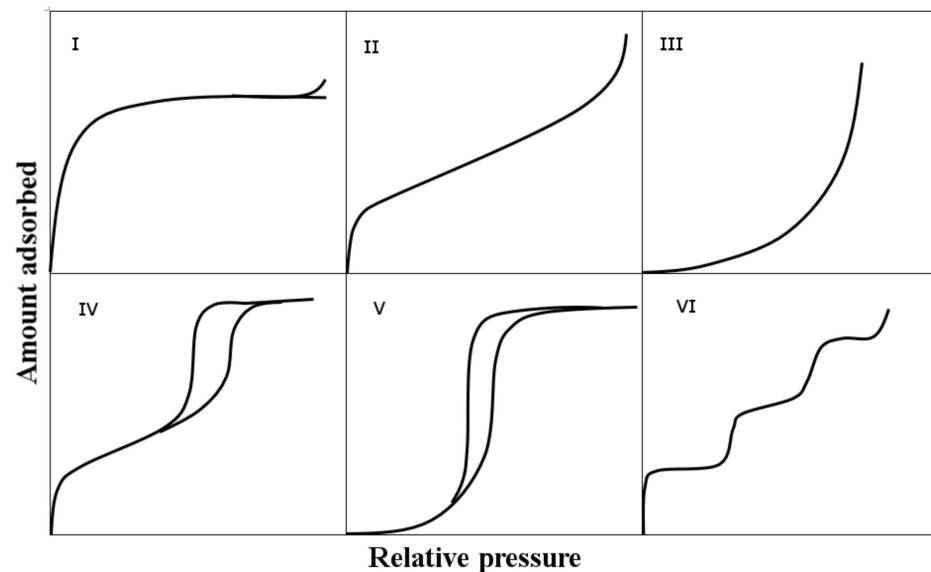


Figure 3. Amount of gas adsorbed as a function of the relative pressure at constant temperature: comparison between representative adsorption models: types I, II, III, IV, V and VI.

To determine the behaviour of the MIL101 in R245fa, gas adsorption experiments were carried out at four different temperatures (10, 25, 40, 60 °C) [41], resulting in the isotherms shown in Figure 4. The uptake is reported as a function of the ratio between the pressure p and the saturation MIL101 pressure p_0 at different adsorption temperatures. Similar experimental analyses were also carried to analyse the desorption behaviour and the resulting curves were almost superimposed with the adsorption ones, confirming the lack of hysteresis in the nanofluid behaviour.

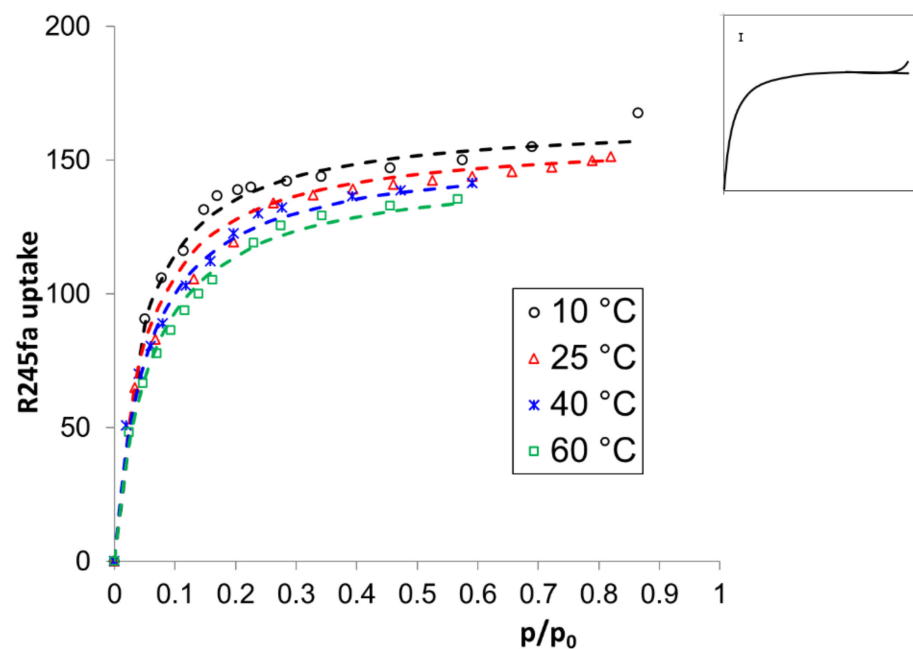


Figure 4. R245fa mass uptake by weight of MIL101 [%] as a function of the relative pressure for four temperature values. Experimental data (coloured circles) and fitting Langmuir model equations.

The comparison between the isotherm shapes in Figure 4 and the adsorption models of Figure 3 identified the R245fa-MIL101 as a type I at all temperatures, as shown for comparison in the Figure 4 on the right. This type is characterized by a monolayer adsorption process [51] which can be modelled by the Langmuir equation [53]:

$$\frac{p}{a} = \frac{p_0}{C \cdot a_m} + \frac{p}{a_m}, \quad (4)$$

where a is the R245fa uptake at pressure p , C is a constant and a_m is the maximum monolayer mass capacity per adsorbent mass unit, which is also constant. More details on the major assumptions of this model can be found in [53].

The value of the constants in the Langmuir equation (C and a_m) were determined by fitting the experimental data at the different temperature values, resulting in the curves reported in Figure 4.

3.1.2. The R245fa/MIL101 Enthalpy of Desorption/Adsorption

The added enthalpy gain Δh_a related to the desorption/adsorption process can be determined by means of the Clausius–Clapeyron equation:

$$\left(\frac{\partial(\ln p)}{\partial\left(\frac{1}{T}\right)} \right)_w = \frac{\Delta h_a}{R}, \quad (5)$$

and it depends on the correlation between pressure p and temperature T , at a certain value of the R245fa molar uptake in the MIL101 molecule w ($R = 62.02 \text{ J/kgK}$ —specific 245fa constant).

According to the Langmuir's model, representing the R245fa/MIL101 nanofluid (Section 3.1.1), the uptake depends on pressure p and temperature T according to the following equation:

$$w \left[\frac{\text{kmol}_{R245fa}}{\text{kg}_{MIL101}} \right] = \frac{2.645 \cdot 10^{-7} \cdot e^{3973.66/T} \cdot p}{1 + 4.586 \cdot 10^{-5} \cdot e^{3758.81/T} \cdot p}, \quad (6)$$

where the correlation coefficients were determined starting from the experimental data [41,42].

The R245fa mass uptake m_{R245fa} by weight of m_{MIL101} dry mass can hence be easily determined with the following equation:

$$\frac{m_{R245fa}}{m_{MIL101}} \left[\frac{\text{kg}_{R245fa}}{\text{kg}_{MIL101}} \right] = w \cdot MM_{R245fa}, \quad (7)$$

where MM_{R245fa} is the R245fa molar mass.

Then, for a number of values of R245fa molar uptake, the enthalpy of desorption Δh_a was determined by means of the Equation (5), resulting in an average value of about 8.7 kcal/mol.

In the case of adsorption, the average absolute value remains the same because of the lack of hysteresis. However, the adsorption process cools down the fluid and hence the enthalpy of adsorption has a negative value (−8.7 kcal/mol) [38,54].

3.2. Nanofluid Modelling Equations: The Heat Exchangers and the Expander

To model the performance of the R245fa/MIL101 nanofluid in an ORC system, it is necessary to adopt equations for estimating the total enthalpy variation in the different components of the system, adding to the conventional enthalpy variation of the pure organic fluid $\Delta h_{2,3}$, with the nanofluid contribution in terms of sensible heat and desorption/adsorption process.

As regards the nanofluid enthalpy increase $\Delta h_{2,3^{nf}}$ in the High Temperature Heat Exchanger (HTHE), the following literature correlation [38] was adopted:

$$h_{3^{nf}} - h_{2^{nf}} = \left[1 + \varphi \left(\frac{\Delta m_{R245fa}}{m_{MIL101}} - 1 \right) \right] \Delta h_{2,3} + \varphi \left[\overline{c_{p,MIL101}} (T_{3^{nf}} - T_2) + \frac{\Delta m_{R245fa}}{m_{MIL101}} \overline{\Delta h_a} \right] \quad (8)$$

where:

- $\varphi = \frac{m_{MIL101}}{m_f}$ is the fraction between the MIL101 mass m_{MIL101} and the total fluid mass m_f ;
- Δm_{R245fa} is the R245 mass uptake difference between the inlet and the outlet of the HTHE determined exploiting Equation (7).
- T_2 and $T_{3^{nf}}$ are the inlet and outlet nanofluid temperature in the HTHE;
- $\overline{c_{p,MIL101}} = 1.1 \frac{J}{g \cdot K}$ is the average MIL101 specific heat capacity in the HTHE defined according to literature values [38,55];
- $\overline{\Delta h_a} = 8.7 \text{ kcal/mol}$ is the average enthalpy of the R245fa/MIL101 desorption process caused by the temperature increase in the HTHE.

Equation (8) was also applied in the low temperature heat exchanger (LTHE), in which the decrease in temperature favors an exothermic adsorption process.

As regards the expander, Equation (8) can also be applied for the definition of the enthalpy variation $\Delta h_{3,4^{nf}}$:

$$h_{4^{nf}} - h_{3^{nf}} = \left[1 + \varphi \left(\frac{\Delta m_{R245fa}}{m_{MIL101}} - 1 \right) \right] \Delta h_{3,4} + \varphi \left[\overline{c_{p,MIL101}} (T_{4^{nf}} - T_{3^{nf}}) + \frac{\Delta m_{R245fa}}{m_{MIL101}} \overline{\Delta h_a} \right] \quad (9)$$

However, its evaluation is more complex due to the conflicting influence of the pressure and temperature variation on the desorbing/adsorbing behaviour of the MIL101 nanoparticles. During the expansion phase, the nanofluid temperature decreases favoring the adsorption process (Figure 1). Simultaneously, the process is accompanied by a pressure decrease which favors the opposite desorption process (Figure 1). Depending on the pressure and temperature variations of the ORC during the expander process, one process prevails on the other, causing a positive/negative enthalpy variation due to the desorption/adsorption process and also affecting the turbine isentropic efficiency. Section 3.4 will show how the process is handled in the optimization procedure.

Equations (8) and (9) clearly show the significant influence of the R245fa mass uptake Δm_{R245fa} on the benefits provided by the nanoparticle suspension. If the mass uptake Δm_{R245fa} is smaller than the mass m_{MIL101} of MIL101 suspended nanoparticles, the term $\left(\frac{\Delta m_{R245fa}}{m_{MIL101}} - 1 \right)$ in Equations (8) and (9) is negative, reducing or even annulling the benefits related to the nanoparticle suspension (second and third terms in Equations (8) and (9)). But the R245fa mass uptake Δm_{R245fa} depends on the operating conditions of the cycle (pressure and temperature values), clearly confirming the need of the optimal tuning of the operating conditions for the nanofluid adoption, as demonstrated in the preliminary analyses [41,42].

3.3. The R245fa-MIL101 Numerical Model: Assumptions and Iterative Procedures

The numerical model developed for the pure fluid (Section 2) was properly modified, introducing the correlations developed for the ORC components (Equations (8) and (9)) in order to take into account the MIL101 nanoparticle suspension in the R245fa fluid.

The complexity of the model requires some simplifying assumptions:

- The R245fa/MIL101 specific heat can be determined by adopting the following equation [56–59]:

$$c_{p,nf} = (1 - \varphi)c_{p,R245fa} + \varphi c_{p,MIL101}, \quad (10)$$

However, since the mass load fraction φ was fixed to be smaller or at most equal to 2% for tackling stability problems and since the MIL101 specific heat ($\overline{c_{p,MIL101}} = 1.1 \frac{kJ}{kg K}$) is smaller than that of the R245fa, the specific nanofluid heat deriving from eq. 7 resulted to have a negligible difference with the R245fa specific heat. For this reason, the following assumption was made:

$$c_{p,nf} \cong c_{p,R245fa}, \quad (11)$$

resulting in an error smaller than 1%.

- Since the specific heat affects the isobar shape in the T-s diagram, the previous assumption (Equation (8)) also allows to consider, for the nanofluid operating points, the same isobars of the pure R245fa fluid during the heat exchanges in the HTHE and in the LTHE.
- In the pumping process, the enthalpy contribution due to the exothermic adsorption process was considered negligible.

In addition to the previous assumptions, it was also necessary to tackle the interdependence between some parameters in the Equations (8) and (9).

In particular, for the HTHE, the outlet temperature $T_{3,nf}$ can be determined once the enthalpy at the outlet $h_{3,nf}$ is known:

$$h_{3,nf} = h_{2,nf} + \Delta h_{2,3,nf}, \quad (12)$$

However, the enthalpy gain $\Delta h_{2,3,nf}$ depends in turn on the outlet temperature $T_{3,nf}$ directly and indirectly via $m_{f ads} = f(p_{evap}, T_{3,nf})$ (Equation (7)). To overcome the problem related to this interdependence, an iterative procedure was developed and included in the numerical model.

The main steps of the procedure are here briefly summarized:

- (1) The R245fa mass uptake at the inlet of the HTHE is determined by applying Equations (6) and (7):

$$w_2 = \frac{2.645 \cdot 10^{-7} \cdot e^{3973.66/T_2} \cdot p_{evap}}{1 + 4.586 \cdot 10^{-5} \cdot e^{3758.81/T_2} \cdot p_{evap}} \frac{m_{R245fa,2}}{m_{MIL101}} [\%] = w_2 \cdot MM_{R245fa}$$

where (T_2, p_{evap}) are the known value of inlet temperature and pressure.

- (2) As regards the outlet, in the first iteration, the outlet nanofluid temperature ($T_{3,nf}$) in the HTHE is assumed equal to the outlet temperature in case of pure fluid R245fa T_3 :

$$T_{3,nf}^{i=0} = T_3$$

- (3) The R245fa mass uptake at the outlet of the HTHE is hence determined:

$$w_{3,nf} = \frac{2.645 \cdot 10^{-7} \cdot e^{3973.66/T_{3,nf}^i} \cdot p_{evap}}{1 + 4.586 \cdot 10^{-5} \cdot e^{3758.81/T_{3,nf}^i} \cdot p_{evap}} \frac{m_{R245fa,3}}{m_{MIL101}} [\%] = w_{3,nf} \cdot MM_{f ads}$$

- (4) The mass desorption and the enthalpy increase between the inlet and the outlet of the HTHE is then calculated:

$$\frac{\Delta m_{f ads}}{m_{MIL101}} = \frac{m_{R245fa,2} - m_{R245fa,3}}{m_{MIL101}}$$

$$\Delta h_{2,3,nf} = \left[1 + \varphi \left(\frac{\Delta m_{wf ads}}{m_{MIL101}} - 1 \right) \right] [\Delta h_{econ} + \Delta h_{evap} + \Delta h_{sh}] + \varphi \left[\overline{c_{p,MIL101}} (T_{3,nf}^i - T_2) + \frac{\Delta m_{wf ads, in}}{m_{MIL101}} \overline{\Delta h_{ads}} \right]$$

- (5) The enthalpy at the outlet of the HTHE is:

$$h_{3,nf} = \Delta h_{2,3nf} + h_2$$

- (6) Starting from the enthalpy and pressure values, it is hence possible to determine the temperature of the nanofluid at the HTHE outlet:

$$T_{3,nf}^* = f(p_{evap}, h_{3,nf})$$

- (7) If this value differs more than 0.1 from the value of the previous iteration i :

$$|T_{3,nf}^* - T_{3,nf}^i| > 0.01$$

the procedure starts again from step 3 by assuming:

$$T_{3,nf}^{i+1} = T_{3,nf}^*$$

Otherwise, it ends.

The same interdependence characterizes the outlet conditions in the expander (T_{4nf} , h_{4nf}) and in the LTHE (T_{5nf} , h_{5nf}). In both cases, once determined the inlet conditions from the previous iteration process, the procedure previously described was adapted and applied for determining the component outlet conditions.

3.4. Optimization Procedure for the Nanofluid

The results obtained by preliminary studies [41] highlighted the promising potential of the MIL101 nanoparticles particularly in terms of area reduction, but did not allow to fully appreciate their potential since the results were affected by two main factors:

- the cycle parameters (pressures, temperatures, etc.) used for the nanofluid were the optimal for the pure fluid and were not tuned to optimize the nanoparticles contribution;
- the influence of the mass fraction loading φ on the nanofluid contribution was not considered.

Therefore, to overcome these issues, the nanofluid model, described in Section 3.4, was included in the optimization procedure to tune the cycle parameters and the nanofluid behaviour. The optimization procedure was aimed at maximizing the power output, through the minimization of the loss in terms of system efficiency η_{syst} :

$$\alpha = 1 - \eta_{syst}, \quad (13)$$

The optimization variables in the procedure (independent variables in Figure 5), were the evaporation pressure p_{evap} , the pinch point temperature differences ($(\Delta T_{pp})_{evap}$, $(\Delta T_{pp})_{cond}$) in both the heat exchangers, the approach point in the HTHE $(\Delta T_{ap})_{evap}$ and the MIL101 mass fraction φ . Whereas the approach point at the condenser $(\Delta T_{ap})_{cond}$ was fixed equal to 25 °C and was included in the optimization procedure together with other input data, listed in Figure 5.

Knowing the input data and by assuming starting values of the optimization variables, the algorithm estimates the first value of the objective function (Equation (13)) following the steps summarized in Figure 5. Then, the optimization algorithm continues searching for the optimal values of the independent variables till the maximum system efficiency is reached.

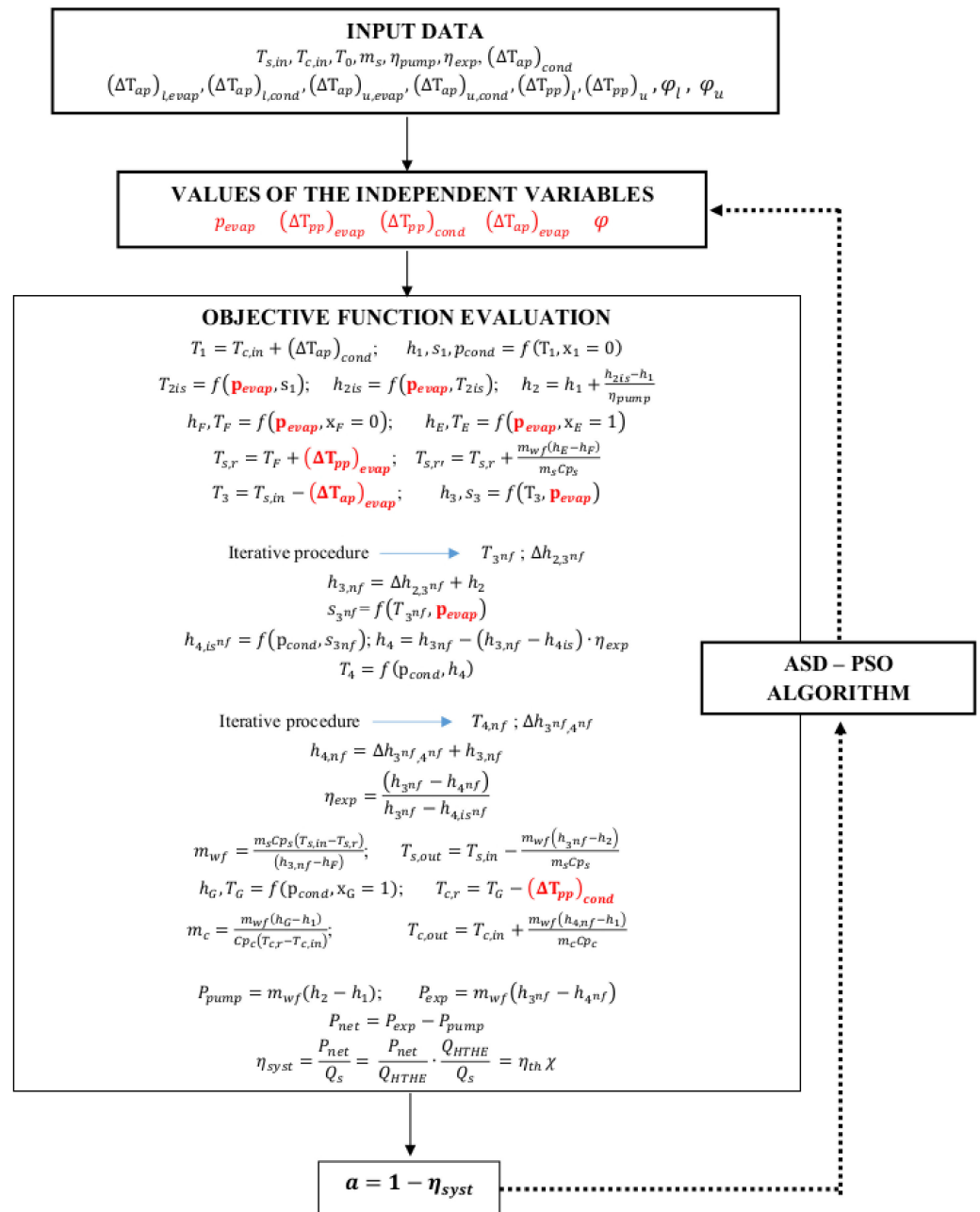


Figure 5. Flow chart of the optimization procedure.

As regards the optimization algorithm, the ASD-PSO, already used in previous ORC optimization analyses [17], was adopted [60].

The limits in the search domain for the optimization variables were fixed as follows:

- the evaporator approach point was assumed to vary from 10 °C to 25 °C and both the evaporator and condenser pinch point varies from 5 °C to 20 °C;
- the evaporation pressure boundaries are driven by several constraints, fixed as follows:
 - the lower bound was defined to ensure the pressure to be always greater than the condensing pressure. Since the approach point at the condenser $(\Delta T_{ap})_{cond}$ and the cold source temperature $T_{c,in}$ were known, the limit was fixed equal to the pressure at a saturation temperature $T_{1,max} = T_{c,in} + (\Delta T_{ap})_{cond}$
 - the upper bound has to guarantee two different conditions: (i) the ORC cycle must be sub-critical and hence the evaporation pressure should be smaller than

the critical pressure by at least 1 bar, as suggested in literature [61]; (ii) the vapour characteristic at the HTHE outlet must be saturated or superheated with an evaporation pressure smaller or at least equal to that at the saturation temperature of $T_{3,min} = T_{s,in} - (\Delta T_{ap})_{evap}$. In order to guarantee both the conditions, the upper bound was fixed equal to the minimum between the two values.

This choice ensures that, even when p_{evap} reaches its maximum value, state point 3 is in the vapour region. The working fluid in state 3 is saturated if $p_{evap} = p_{evap,max}$ and superheated in the other cases.

- the mass fraction load (φ) of nanoparticles was supposed to vary between 0.05% and 2%: the minimum value of the mass fraction load was fixed to have a minimum impact of the MIL101 on the pure fluid performance, whereas the maximum value was fixed to avoid stability problems according to previous studies on the topic [62].

4. Results

To analyse the influence of the heat source temperature on the R245fa/MIL101 contribution, optimization analyses were carried out at five different heat source temperatures (from 100 °C to 150 °C). The cycle parameters were optimized to maximize the system efficiency and the results achieved by the nanofluid R245+MIL101 were then compared with those achieved by the pure fluid.

First, as expected, the different behaviours of the two fluids (pure fluid vs. nanofluid) result in optimized operating cycles with slightly different values of some parameters. This is clear, for example, in Figure 6, comparing the optimized cycles in the T-s diagram, and confirms the need of the developing a numerical model for optimizing the nanofluids performance.

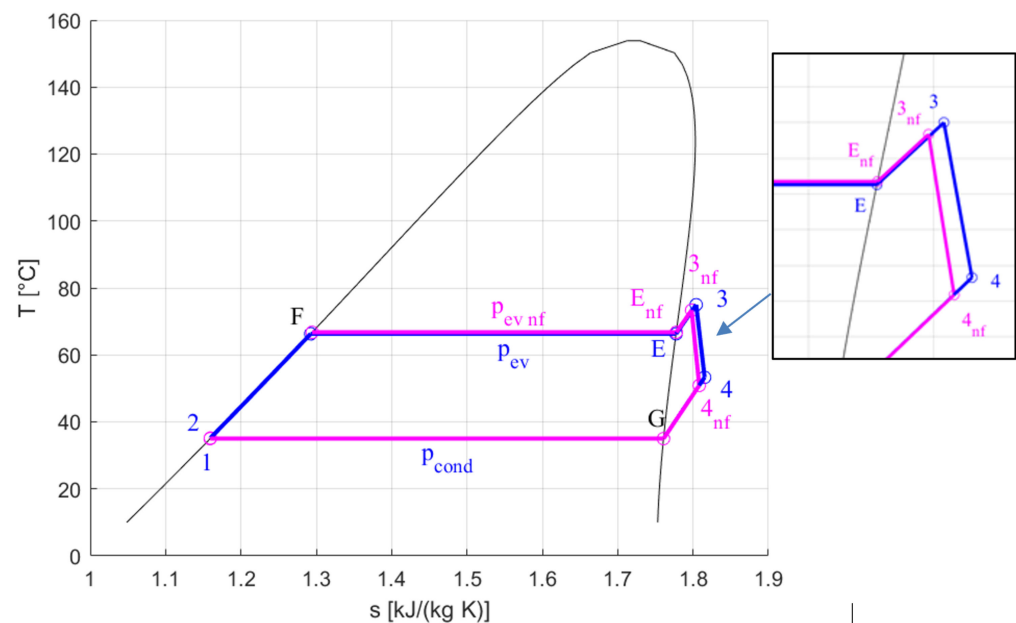


Figure 6. Comparison between the expansion of the pure R245fa (blue line) and of the R245fa/MIL101 nanofluid (pink line) in the T-s diagram ($T_{s,in} = 100$ °C).

As regards the numerical results (Tables 1 and 2), for the same heat source temperatures, the introduction of nanoparticles in R245fa resulted in higher net power output especially when considering ultra-low heat source temperature (+2.9% for 100 °C, +2.3% for 110 °C, +1.7% for 120 °C).

Table 1. Results of the optimization of the ORC with R245fa + MIL101 as working fluid for the considered hot source temperatures.

$T_{s,in}$ [°C]	P_{ev} [bar]	$\Delta T_{ap,ev}$ [°C]	$\Delta T_{pp,ev}$ [°C]	$\Delta T_{pp,cond}$ [°C]	φ [%]	η_{syst} [%]	P_{net} [kW]	χ [%]	η_{th} [%]
100	5.58	25	5	8.9	2.00%	2.84%	50.52	41.72%	6.81%
110	6.52	25	5	19.7	2.00%	3.43%	68.21	44.46%	7.72%
120	7.63	25	5	6.7	2.00%	4.02%	88.38	46.85%	8.58%
130	10.48	25	5	5.4	2.00%	4.52%	108.77	43.55%	10.38%
140	10.48	25	5	5.4	2.00%	5.20%	136.11	50.86%	10.23%
150	12.37	25	5	5.6	2.00%	5.80%	163.78	52.54%	11.03%

Table 2. Results of the optimization of the ORC with R245fa as working fluid for the considered heat source temperatures.

$T_{s,in}$ [°C]	P_{ev} [bar]	$\Delta T_{ap,ev}$ [°C]	$\Delta T_{pp,ev}$ [°C]	$\Delta T_{pp,cond}$ [°C]	φ [%]	η_{syst} [%]	P_{net} [kW]	χ [%]	η_{th} [%]
100	5.51	25	5	13.9	-	2.76%	49.1	42.14%	6.55%
110	6.42	25	5	20	-	3.35%	66.69	45.00%	7.45%
120	7.46	25	5	5.1	-	3.95%	86.9	47.53%	8.32%
130	10.13	25	5	5.7	-	4.48%	107.75	44.72%	10.01%
140	10.13	25	5	5.7	-	5.17%	135.24	51.85%	9.97%
150	11.87	25	5	5	-	5.79%	163.47	53.76%	10.77%

This positive contribution is achieved by maximizing the mass load fraction φ which is always equal to the maximum value (2%) in the allowed range (0.5–2%). However, this contribution becomes lower and lower for increasing heat source temperatures and, at a certain point, is of the same order of the model uncertainty (0.2% for 150 °C). To explain these results, it is necessary to enter into the details of the behaviour of the working fluid.

For the pure fluid, at a fixed heat source temperature, the optimization algorithm searches for the best compromise between two conflicting aspects: on one side, the need of limiting the value of the evaporation pressure in order to maximize the heat recovery efficiency and, on the other side, the need of maximizing the enthalpy drop (by increasing the evaporation pressure) to maximize the thermal efficiency.

In the case of the nanofluid, there are other two contributions to account for:

- the endothermic desorption process of the MOHCs, which decreases for increasing evaporation pressure values;
- the increase in expander efficiency for increasing evaporation pressure.

As a consequence of the thermodynamic behaviour of MOHC, the entropy of the system is affected by the occurrence of desorption/adsorption processes [40]. In particular, when the adsorption process takes place, the total entropy of the system is reduced. This could happen in the expander, where the temperature decrease favours the R245fa adsorption. If the pressure conditions, also affecting the R245fa uptake, are favourable, the adsorption process limits the entropy increase during the expansion, with a slight increase in expander isentropic efficiency and benefits for the overall efficiency [38]. This is clear in Table 3 reporting the resulting values of the expander efficiencies because of the adsorption process in the optimization analyses for the different heat source temperatures.

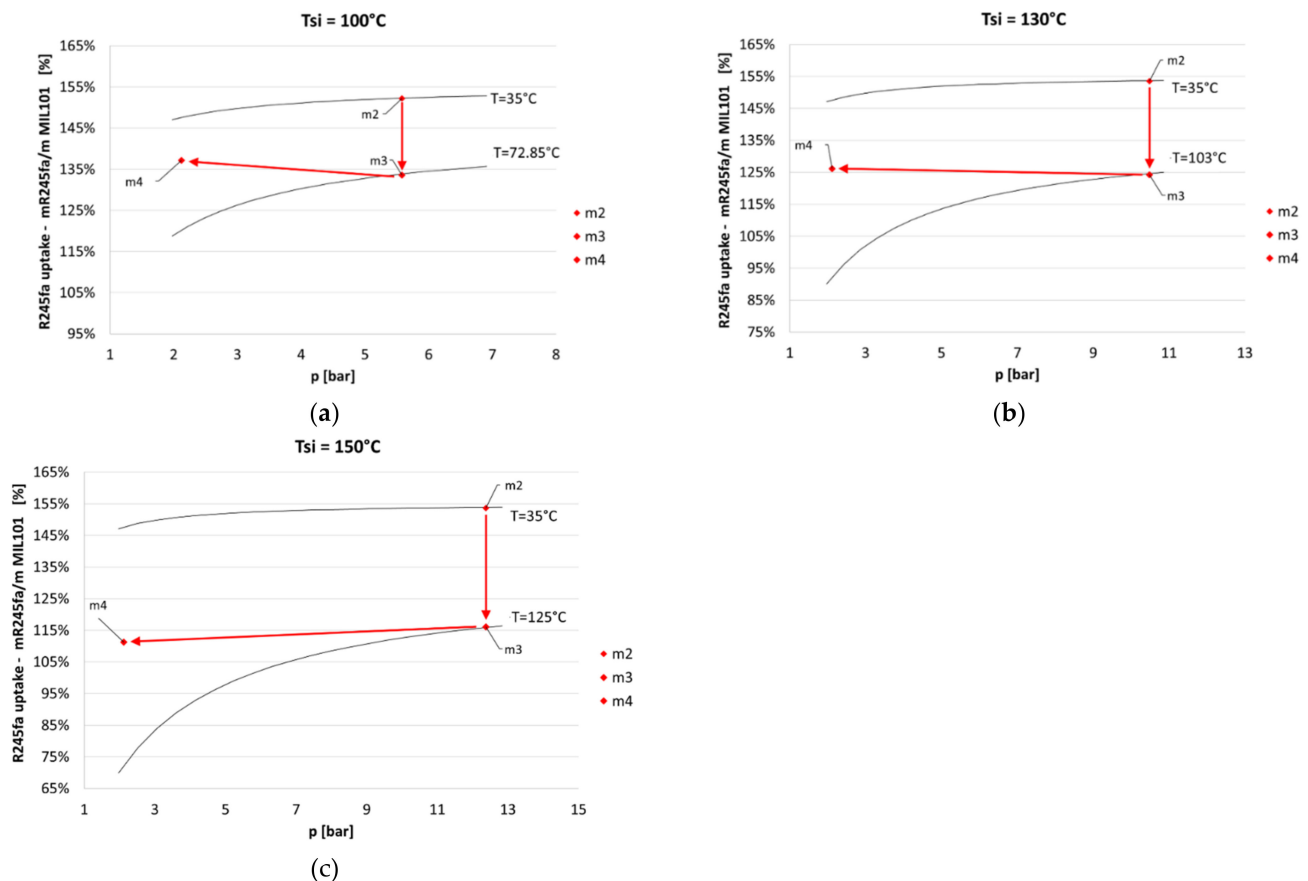
Among these two further contributions, the second one seems to be predominant, and this explains why, in the nanofluid case, the optimized cycle is characterized by evaporation pressure values from 1% to 4% higher than those of the pure fluid (Tables 1 and 2). Therefore, the enthalpy drops increase, allowing to achieve higher thermal efficiency η_{syst} but lower heat recovery efficiency χ (1% to 2%).

Table 3. Isentropic expander efficiency: optimization results at the considered heat source temperatures.

$T_{s,in}$ [°C]	$\eta_{exp,nf}$ [%]
100	82.04%
110	81.63%
120	81.25%
130	81.41%
140	80.59%
150	80.34%

However, at increasing heat source temperatures, the MOHC desorption contribution further decreases because of the increase in the evaporation pressure but this decrease is not compensated by the MOHC adsorption contribution due to the unfavourable pressure and temperature values in the first part of the expansion process.

This is clearly seen in Figure 7, which presents the uptake of R245fa in MIL101 at the inlet of the HTHE (point 2) and at the expander inlet and outlet (points 3 and 4) for heat sources of 100 °C, 130 °C and 150 °C.

**Figure 7.** Uptake at the inlet of the HTHE (point 2) and at the expander inlet and outlet (points 3 and 4) for heat sources of 100 °C (a), 130 °C (b) and 150 °C (c).

In all the three cases, at the HTHE the uptake always decreases (Figure 7): indeed, during the heat transfer at constant pressure, the temperature raises and thus, considering the experimental adsorption isotherms (Figure 4), desorption occurs allowing to extract extra heat at the heat source.

At the expander, pressure and temperature induce opposite effects on the uptake. While the pressure drop induces desorption, the temperature decrease induces adsorption,

which is preferable in the expander since it makes the expansion process more isentropic and the enthalpy drop greater.

As it can be seen, for heat source temperatures of 100 °C and 130 °C (Figure 8a,b), adsorption occurs ($m_{f ads,3} < m_{f ads,4}$), allowing enthalpy drops and thus power outputs greater than those with the pure fluid.

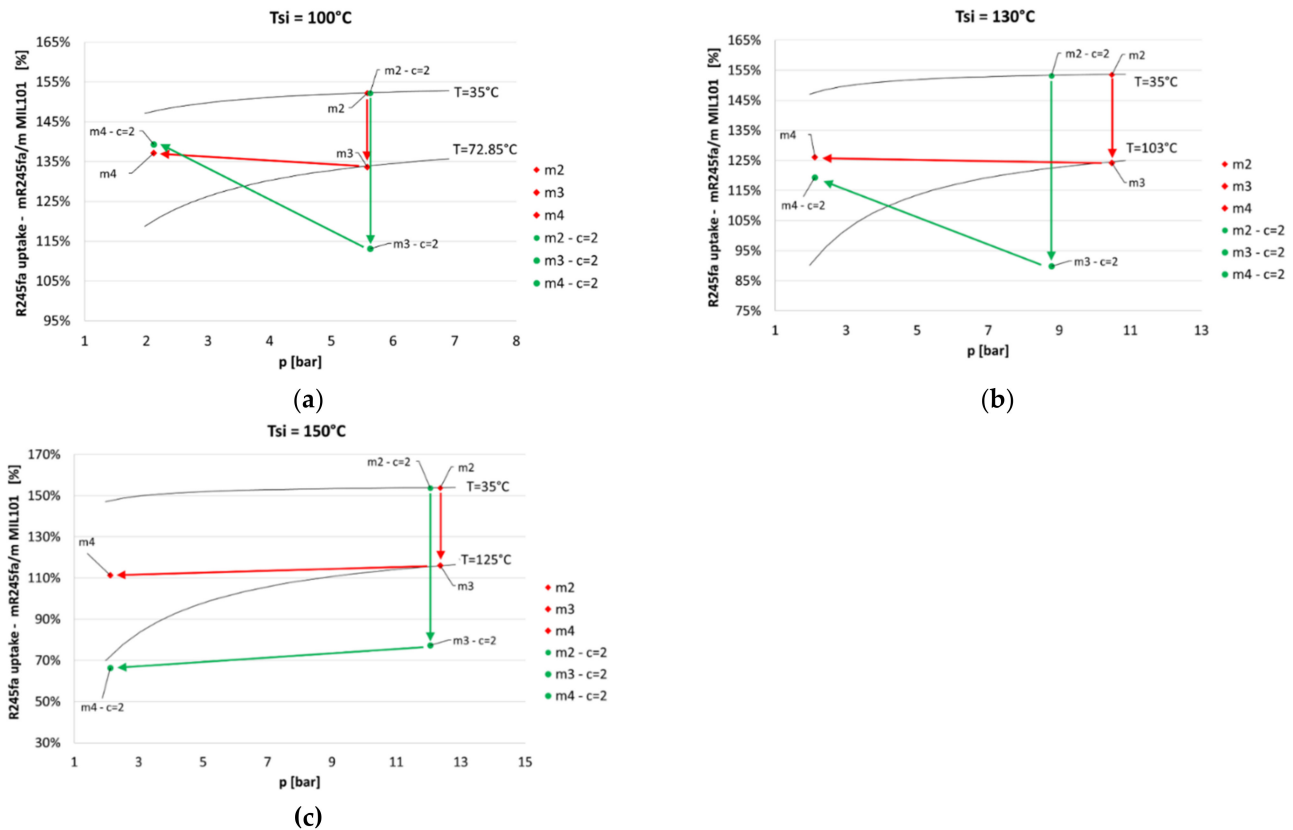


Figure 8. Comparison between the MIL101 (red) uptake and a theoretic MIL101 (green) with double uptake in the optimal conditions for heat source temperatures of 100 °C (a), 130 °C (b) and 150 °C (c).

For 140 °C and higher temperatures (Figure 8c), because of the unfavourable pressure and temperature variations, desorption occurs at the expander ($m_{f ads,3} > m_{f ads,4}$). Because of this, the positive contribution of the MOHC nanoparticles becomes almost negligible, with a performance increase of the same order of the model uncertainty (0.2% for 150 °C).

This behaviour is also reflected in the expander efficiency values (Table 3). The increase in the expander efficiency compared to the assumed starting value of pure fluid in expander design operating condition (80%) is not negligible at ultra-low heat source temperatures (+2.4% for 100 °C, +1.63% for 110 °C), but becomes less significant for 140 °C (+0.59%) and almost negligible for 150 °C (+0.34%). Thus, the results obtained shows that the nanofluid influence is more effective when the source temperature is particularly low (<130 °C).

Double Uptake Scenario

Research on nanofluids is still ongoing and new improved nanoparticles are and will be synthesized. Since the year 2000s, where the first experimental studies were conducted more than 2000 publications on experimental studies with nanofluids have been presented, of which more than 50% have appeared during the last 5 years [63].

In this section, a scenario considering a theoretical nanoparticle doubling the amount of working fluid adsorbed or desorbed compared to MIL101, is not impossible and is here considered in order to appreciate the influence of enhanced uptake capability in the improvement of the ORC technology performance.

To account for this scenario, the same numerical model presented in Section 3.4 has been adopted, but a double amount of desorbed/adsorbed mass was hypothesized, by modifying Equation (6) as follows:

$$w \left[\frac{\text{kmol}_f, \text{ads}}{\text{kg}_{\text{MOHC}}} \right] = c \cdot \frac{2.645 \cdot 10^{-7} \cdot e^{3973.66/T} \cdot p}{1 + 4.586 \cdot 10^{-5} \cdot e^{3758.81/T} \cdot p'} \quad (14)$$

where $c = 2$.

With these enhanced uptake properties of the MOHC nanoparticles, the optimization was carried out again and the results are presented in Table 4. The positive influence of the nanofluid on the ORC efficiency is confirmed up to the heat source temperature of 120 °C, with a maximum increase in system performance for 100 °C (50.83 kW, +3.51% compared to optimal pure fluid). However, the enhanced adsorption/desorption nanofluid processes are limited at low temperatures (+0.11% compared to the standard MIL101 for 100 °C) and become even detrimental for heat source temperatures greater than 120 °C (system efficiency always smaller than that of the standard MIL101).

Table 4. Results of the optimization of the ORC with R245fa + MIL101 considering a theoretical double uptake ($c = 2$).

$T_{s,in}$ [°C]	P_{ev} [bar]	$\Delta T_{ap,ev}$ [°C]	$\Delta T_{pp,ev}$ [°C]	$\Delta T_{pp,cond}$ [°C]	φ [%]	η_{syst} [%]	P_{net} [kW]	χ [%]	η_{th} [%]
100	5.63	25	5	5.1	2.00%	2.86%	50.83	41.28%	6.92%
110	6.6	25	5	19.9	2.00%	3.43%	68.17	43.87%	7.82%
120	7.75	25	5	6.9	2.00%	3.99%	87.76	46.09%	8.66%
130	8.78	25	5	20	0.50%	4.56%	109.76	49.42%	9.23%
140	10.26	25	5	5.4	0.50%	5.16%	134.95	51.40%	10.03%
150	12.05	25	5	5.3	0.50%	5.76%	162.76	53.18%	10.83%

To understand the reason of these results, the uptake of the enhanced MOHC particles is compared with that of the standard MIL101 during the evaporation and expansion processes (Figure 8).

It is clear that the general trend of the adsorption/desorption process is similar for both the theoretical and the enhanced nanofluid. In both cases, in the HTHE the nanofluid experiences a desorption process, whereas in the expander an adsorption process only occurs up to a heat source temperature of 130 °C.

However, despite this similar trend, a non-negligible difference emerges: the boosted desorption process increases the temperature values at the end of the evaporation process and at the beginning of the expander process. Despite these increased values, for heat source temperatures lower than 120 °C, the temperature and pressure evolution during the expansion phase favours a strong adsorption process, resulting in enthalpy drops and isentropic efficiencies higher than those of the standard MIL101. As a result, in these cases the performance of the theoretical nanofluid is slightly better or at least comparable with those of the standard MIL101.

On the contrary, for heat source temperatures greater than 120 °C, the desorption process in the HTHE causes a too significant increase in the outlet temperature, negatively affecting the following adsorption process in the expander. Because of this, at the outlet of the expander the temperature T_4 is still high and the final uptake value is smaller than that of the standard MIL101. So, for these heat source temperatures, the enhanced adsorption/desorption properties of the nanofluid, combined with the unfavorable high evaporation pressure values (characterizing these operating conditions), negatively affect the ORC performance.

In order to mitigate this negative influence, the optimization algorithm minimizes the mass loading fraction ($\varphi = 0.5\%$) and lowers the evaporation pressure p_{ev} even below that of the pure fluid (8.78 bar vs. 10.48 bar, -13.37% for $T_{s,i} = 130$ °C) so as to push on the

increase in the heat recovery efficiency. Nevertheless, the power output turns out to be lower than that of the standard MIL101 (-1.15% for $T_{s,i} = 130\text{ }^{\circ}\text{C}$; -0.20% for $T_{s,i} = 140\text{ }^{\circ}\text{C}$; -0.20% for $T_{s,i} = 150\text{ }^{\circ}\text{C}$).

In conclusion, the doubled uptake scenario is not promising in terms of enhancement of the nanofluid performance in an ORC system and further enhancement of the nanofluid properties are not supposed to pursue an increase in the uptake capability, at least for heat source temperatures greater than $120\text{ }^{\circ}\text{C}$.

5. Conclusions

The possibility of recovering the large amount of low-grade heat, which is wasted nowadays, certainly represents a significant target for supporting the transition towards a climate neutral society. However, despite the huge potential, the most promising technologies, such as ORCs, are still not able to successfully exploit it due to the negative influence of the low grade of the heat source temperature on the system efficiency.

To deal with this low grade, nanofluids have been more than once suggested as a promising solution. However, in similar applications, standard nanoparticles have proven not to perform as well as expected.

To overcome this issue, molecular engineers have suggested the possible use of the metal organic heat carrier (MOHC) nanoparticles, capable of extracting not only the nanoparticle sensible heat but also a second contribution due to the endothermic desorption process from the MOHC porous structure.

In this paper, to assess the potential gain deriving from the MOHC application, a MOHC-based nanofluid was investigated, i.e., the R245fa/MIL101. Since the uptake capacity of the porous structure depends not only on the operating conditions (pressure and temperature values) but also on the pure fluid characteristics and on its matching with the structure of the adopted MOHC, the adsorption/desorption process of the R245fa in the MIL101 was experimentally investigated and proper correlations were defined for modelling the nanofluid behaviour in the ORC components. Then, the nanofluid model was included in the optimization procedure to tune the cycle parameters and the nanofluid behaviour with the aim of maximizing the net power output.

Optimization analyses were carried out at five different heat source temperatures (from $100\text{ }^{\circ}\text{C}$ to $150\text{ }^{\circ}\text{C}$). The cycle parameters were optimized to maximize the system efficiency and the results achieved by the nanofluid R245+MIL101 were then compared with those achieved by the pure fluid.

The comparison brought to the following conclusions:

- The introduction of the MIL101 nanoparticles in the pure fluid R245fa resulted in higher net power output especially when considering ultra-low heat source temperature ($+2.9\%$ for $100\text{ }^{\circ}\text{C}$, $+2.3\%$ for $110\text{ }^{\circ}\text{C}$, $+1.7\%$ for $120\text{ }^{\circ}\text{C}$).
- The main reason of the higher net power output is the increase in expander efficiency due to the adsorption process limiting the entropy increase during the expansion ($+2.04\%$ for $100\text{ }^{\circ}\text{C}$, $+1.63\%$ for $110\text{ }^{\circ}\text{C}$, $+1.25\%$ for $120\text{ }^{\circ}\text{C}$, $+1.41\%$ for $130\text{ }^{\circ}\text{C}$).
- The need of tuning the system thermodynamic operating conditions and the nanofluid behaviour is confirmed by the different evaporation pressure values characterizing the nanofluid case: from 1% to 4% higher than those of the pure fluid.
- For heat source temperatures higher than $120\text{ }^{\circ}\text{C}$, the constraints of the thermodynamic cycle force to have higher evaporation pressure. This creates unfavorable pressure and temperature values in the expansion, resulting in a desorption process and an almost negligible contribution of the MOHC nanoparticles ($+0.2\%$ of net power output for $130\text{ }^{\circ}\text{C}$). To overcome the constraints.
- As regards the MIL101 mass volume fraction φ , the maximum allowed value (2%) turned out to be beneficial for the system performance. However, mass volume fractions higher than 2% are at the time being not feasible due to technical limits. Above all, stability and deposit issues are still far from being fully solved in a challenging

environment as an ORC system, in which the nanofluid passes through not only heat exchangers but also fluid machines for thousands of operating cycles.

To trace the path for further MIL101 enhancement by molecular engineering, further analyses considering a theoretical enhancement of the adsorption/desorption attitude of the MOHC were carried out. However, the improvements achieved were almost negligible at 100 °C, so discouraging to pursue this research direction.

In terms of future developments, even if MOHC-based nanofluids have a clear potential of increasing the ORC efficiency in waste heat recovery applications, their successful application requires an optimal tuning between the heat source temperature and the nanofluid behavior. To do this, it will be necessary to:

- Experimentally analyze the adsorption/desorption processes for different combination of pure fluids and MOHC nanoparticles allowing to model the each MOHC-based nanofluid by means of semi-empirical correlations;
- Experimentally investigate the stability and the performance of MOHC-based nanofluid in fluid machines, i.e., expanders and pumps, so as to improve the numerical models.
- Numerically identify the perfect combination between pure fluid and MOHC nanoparticle depending on the heat source temperature

Author Contributions: Conceptualization, G.C.; Methodology, G.C.; Software, S.B. and G.C.; Validation, G.C.; Formal analysis, G.C.; Investigation, G.C. and S.B., resources, G.C., Data curation, G.C. and S.B.; Writing—original draft, G.C.; writing—review and editing, G.C.; Visualization, S.B.; Supervision, G.C.; project administration, G.C. All authors have read and agreed to the published version of the manuscript.

Funding: This research received no external funding.

Informed Consent Statement: Not applicable.

Acknowledgments: The authors would like to thank Peter McGrail from the Pacific Northwest National Laboratory for his helpful advice on the modelling of the nanofluid behaviour in the ORC cycles.

Conflicts of Interest: The authors declare no conflict of interest.

Nomenclature

Symbols:

c_p	Heat Capacity at constant pressure	[kJ/kg K]
f	Objective function	[m ² /kW]
h	Enthalpy	[kJ/kg]
m	Mass	[g]
\dot{m}	Mass flow rate	[kg/s]
MM	Molar Mass	[kg/kmol]
p	Pressure	[kPa]
P	Power	[kW]
Q	Heat Power	[kW]
R	molar gas constant	[J/K·mol]
S	Entropy	[kJ/°C mol]
T	Temperature	[°C]
w_i	Adsorbate molar uptake per unit of adsorbent mass	[kmol/kg]
U	Heat transfer coefficient	[W/m ² K]
Δh_a	Enthalpy of adsorption/desorption	[kJ/kg]
ΔT	Temperature difference	[°C]

Greek Letters:

η	Efficiency	[-]
ϕ	Nanoparticle mass fraction loading in the nanofluid	[-]
ρ	Density	[kg/m ³]
χ	Heat Recovery efficiency	[-]

Superscripts and Subscripts:

ads	adsorbed
ap	Approach Point
c	Cold source
cond	Condenser
desup	desuperheater
econ	economizer
evap	Evaporator
exp	Expander
f	Organic fluid
in	Inlet
is	Isentropic
net	Net
nf	Nanofluid
out	Outlet
pp	Pinch Point
pump	Pump
s	Heat source fluid
sh	Superheater
syst	System
th	Thermal
tot	Total
wf	Working fluid

References

1. IEA. *Industrial Excess Heat Recovery-Technologies and Applications-Annex XV*; International Energy Agency: Paris, France, 2015.
2. Brückner, S.; Liu, S.; Miró, L.; Radspieler, M.; Cabeza, L.F.; Lävemann, E. Industrial waste heat recovery technologies: An economic analysis of heat transformation technologies. *Appl. Energy* **2015**, *151*, 157–167. [[CrossRef](#)]
3. Lian, H.; Li, Y.; Shu, G.; Gu, C. An Overview of Domestic Technologies for Waste Heat Utilization. *Energy Conserv. Technol.* **2011**, *29*, 123–128.
4. Tchanche, B.F.; Lambrinos, G.; Frangoudakis, A.; Papadakis, G. Low-grade heat conversion into power using organic Rankine cycles—A review of various applications. *Renew. Sustain. Energy Rev.* **2011**, *15*, 3963–3979. [[CrossRef](#)]
5. Huang, F.; Zheng, J.; Baleynaud, J.M.; Lu, J. Heat recovery potentials and technologies in industrial zones. *J. Energy Inst.* **2017**, *90*, 951–961. [[CrossRef](#)]
6. Turgut, M.S.; Turgut, O.E. Multi-objective optimization of the basic and single-stage Organic Rankine Cycles utilizing a low-grade heat source. *Heat Mass Transf.* **2019**, *55*, 353–374. [[CrossRef](#)]
7. Tocci, L.; Pal, T.; Pasmazoglou, I.; Franchetti, B. Small Scale Organic Rankine Cycle (ORC): A Techno-Economic Review. *Energies* **2017**, *10*, 413. [[CrossRef](#)]
8. Cao, M.; Yang, X.; Wang, J.; Zhang, X.; Guo, H. Economic Analysis of Organic Rankine Cycle Using R123 and R245fa as Working Fluids and a Demonstration Project Report. *Appl. Sci.* **2019**, *9*, 288.
9. Lakew, A.A.; Bolland, O. Working fluids for low-temperature heat source. *Appl. Therm. Eng.* **2010**, *30*, 1262–1268. [[CrossRef](#)]
10. Zhao, L.; Bao, J. Thermodynamic analysis of organic Rankine cycle using zeotropic mixtures. *Appl. Energy* **2014**, *130*, 748–756. [[CrossRef](#)]
11. Wang, D.; Ling, X.; Peng, H.; Liu, L.; Tao, L. Efficiency and optimal performance evaluation of organic Rankine cycle for low grade waste heat power generation. *Energy* **2013**, *50*, 343–352. [[CrossRef](#)]
12. Saleh, B.; Koglbauer, G.; Wendland, M.; Fischer, J. Working fluids for low-temperature organic Rankine cycles. *Energy* **2007**, *32*, 1210–1221. [[CrossRef](#)]
13. Chen, H.; Goswami, D.Y.; Stefanakos, E.K. A review of thermodynamic cycles and working fluids for the conversion of low-grade heat. *Renew. Sustain. Energy Rev.* **2010**, *14*, 3059–3067. [[CrossRef](#)]
14. He, C.; Liu, C.; Zhou, M.; Xie, H.; Xu, X.; Wu, S.; Li, Y. A new selection principle of working fluids for subcritical organic Rankine cycle coupling with different heat sources. *Energy* **2014**, *68*, 283–291. [[CrossRef](#)]
15. Xu, J.; Yu, C. Critical temperature criterion for selection of working fluids for subcritical pressure Organic Rankine cycles. *Energy* **2014**, *74*, 719–733. [[CrossRef](#)]
16. Li, X.; Zhao, W.; Lin, D.; Zhu, Q. Working fluid selection based on critical temperature and water temperature in organic Rankine cycle. *Sci. China Technol. Sci.* **2015**, *58*, 138–146. [[CrossRef](#)]
17. Cavazzini, G.; Bari, S.; Pavesi, G.; Ardizzon, G. A multi-fluid PSO-based algorithm for the search of the best performance of sub-critical Organic Rankine Cycles. *Energy* **2017**, *129*, 42–58. [[CrossRef](#)]

18. Choi, S.U.S.; Eastman, J.A. Enhancing thermal conductivity of fluids with nanoparticles. In Proceedings of the ASME International Mechanical Engineering Congress & Exposition, San Francisco, CA, USA, 12–17 November 1995.
19. Choi, S.U.S.; Zhang, Z.G.; Yu, W.; Lockwood, F.E.; Grulke, E.A. Anomalous thermal conductivity enhancement in nanotube suspensions. *Appl. Phys. Lett.* **2001**, *79*, 2252–2254. [[CrossRef](#)]
20. Michaelides, E.E. *Nanofluidics*; Springer: Cham, Switzerland, 2014. [[CrossRef](#)]
21. Godson, L.; Raja, B.; Mohan Lal, D.; Wongwises, S. Enhancement of heat transfer using nanofluids-An overview. *Renew. Sustain. Energy Rev.* **2010**, *14*, 629–641. [[CrossRef](#)]
22. Saidur, R.; Leong, K.Y.; Mohammad, H. A review on applications and challenges of nanofluids. *Renew. Sustain. Energy Rev.* **2011**, *15*, 1646–1668. [[CrossRef](#)]
23. Martinez, J.O.; Brown, B.S.; Quattrocchi, N.; Evangelopoulos, M.; Ferrari, M.; Tasciotti, E. Multifunctional to multistage delivery systems: The evolution of nanoparticles for biomedical applications. *Chin. Sci. Bull.* **2012**, *57*, 3961–3971. [[CrossRef](#)]
24. Mousavi Ajarostaghi, S.S.; Zaboli, M.; Javadi, H.; Badenes, B.; Urchueguia, J.F. A Review of Recent Passive Heat Transfer Enhancement Methods. *Energies* **2022**, *15*, 986. [[CrossRef](#)]
25. Bellos, E.; Tzivanidis, C. Thermal analysis of parabolic trough collector operating with mono and hybrid nanofluids. *Sustain. Energy Technol. Assess.* **2018**, *26*, 105–115. [[CrossRef](#)]
26. Mahian, O.; Kianifar, A.; Sahin, A.Z.; Wongwises, S. Entropy generation during Al₂O₃/water nanofluid flow in a solar collector: Effects of tube roughness, nanoparticle size, and different thermophysical models. *Int. J. Heat Mass Transf.* **2014**, *78*, 64–75. [[CrossRef](#)]
27. Abdalha Mahmood, A.H.; Hussain, M.I.; Lee, G.-H. Effects of Nanofluids in Improving the Efficiency of the Conical Concentrator System. *Energies* **2022**, *15*, 28. [[CrossRef](#)]
28. Kumaresan, G.; Sudhakar, P.; Santosh, R.; Velraj, R. Experimental and numerical studies of thermal performance enhancement in the receiver part of solar parabolic trough collectors. *Renew. Sustain. Energy Rev.* **2017**, *77*, 1363–1374. [[CrossRef](#)]
29. De Risi, A.; Milanese, M.; Laforgia, D. Modelling and optimization of transparent parabolic trough collector based on gas-phase nanofluids. *Renew. Energy* **2013**, *58*, 134–139. [[CrossRef](#)]
30. Mahian, O.; Kianifar, A.; Zeinali Heris, S.; Wen, D.; Sahin, A.; Wongwises, S. Nanofluids effects on the evaporation rate in a solar still equipped with a heat exchanger. *Nano Energy* **2017**, *36*, 134–155. [[CrossRef](#)]
31. Habibi, H.; Zoghi, M.; Chitsaz, A.; Javaherdeh, K.; Ayazpour, M. Thermo-economic performance comparison of two configurations of combined steam and organic Rankine cycle with steam Rankine cycle driven by Al₂O₃-therminol VP-1 based PTSC. *Sol. Energy* **2019**, *180*, 116–132. [[CrossRef](#)]
32. Toghyani, S.; Baniasadi, E.; Afshari, E. Thermodynamic analysis and optimization of an integrated Rankine power cycle and nano-fluid based parabolic trough solar collector. *Energy Convers. Manag.* **2016**, *121*, 93–104. [[CrossRef](#)]
33. Bellos, E.; Tzivanidis, C. Parametric analysis and optimization of an Organic Rankine Cycle with nanofluid based solar parabolic trough collectors. *Renew. Energy* **2017**, *114*, 1376–1393. [[CrossRef](#)]
34. Bellos, E.; Tzivanidis, C. Optimization of a solar-driven trigeneration system with nanofluid-based parabolic trough collectors. *Energies* **2017**, *10*, 848. [[CrossRef](#)]
35. Alam, T.; Balam, N.B.; Kulkarni, K.S.; Siddiqui, M.I.H.; Kapoor, N.R.; Meena, C.S.; Kumar, A.; Cozzolino, R. Performance Augmentation of the Flat Plate Solar Thermal Collector: A Review. *Energies* **2021**, *14*, 6203. [[CrossRef](#)]
36. Loni, R.; Askari Asli-Ardeh, E.; Ghobadian, B.; Najafi, G.; Bellos, E. Effects of size and volume fraction of alumina nanoparticles on the performance of a solar organic Rankine cycle. *Energy Convers. Manag.* **2019**, *182*, 398–411. [[CrossRef](#)]
37. Jin, X.; Lin, G.; Jin, H.; Fu, Z.; Sun, H. Experimental Research on the Selective Absorption of Solar Energy by Hybrid Nanofluids. *Energies* **2021**, *14*, 8186. [[CrossRef](#)]
38. McGrail, B.P.; Thallapally, P.K.; Blanchard, J.; Nune, S.K.; Jenks, J.W.J.; Dang, L.X. Metal-organic heat carrier nanofluids. *Nano Energy* **2013**, *2*, 845–855. [[CrossRef](#)]
39. Ferey, G. A Chromium Terephthalate-Based Solid with Unusually Large Pore Volumes and Surface Area. *Science* **2005**, *310*, 1119. [[CrossRef](#)]
40. Chen, C.; Zhang, M.; Guan, Q.; Li, W. Kinetic and thermodynamic studies on the adsorption of xylenol orange onto MIL-101(Cr). *Chem. Eng. J.* **2012**, *183*, 60–67. [[CrossRef](#)]
41. Cavazzini, G.; Bari, S.; McGrail, P.; Benedetti, V.; Pavesi, G.; Ardizzon, G. Contribution of Metal-Organic-Heat Carrier nanoparticles in a R245fa low-grade heat recovery Organic Rankine Cycle. *Energy Convers. Manag.* **2019**, *199*, 111960. [[CrossRef](#)]
42. Cavazzini, G.; Bari, S.; Benedetti, V.; McGrail, P.; Pavesi, G.; Ardizzon, G. Influence of the use of Innovative Nanofluid on net power production in ORCs for low-grade waste heat recovery applications. In Proceedings of the 5th International Seminar on ORC Power Systems, Athens, Greece, 9–11 September 2019.
43. Cavazzini, G.; Dal Toso, P. Techno-economic feasibility study of the integration of a commercial small-scale ORC in a real case study. *Energy Convers. Manag.* **2015**, *99*, 161–175. [[CrossRef](#)]
44. Avadhanula, V.K.; Lin, C.-S. Empirical Models for a Screw Expander Based on Experimental Data from Organic Rankine Cycle System Testing. *J. Eng. Gas Turbines Power* **2014**, *136*, 062601. [[CrossRef](#)]
45. Khennich, M.; Galanis, N. Optimal Design of ORC Systems with a Low-Temperature Heat Source. *Entropy* **2012**, *14*, 370–389. [[CrossRef](#)]

46. Quoilin, S.; Aumann, R.; Grill, A.; Schuster, A.; Lemort, V.; Spliethoff, H. Dynamic modeling and optimal control strategy of waste heat recovery Organic Rankine Cycles. *Appl. Energy* **2011**, *88*, 2183–2190. [[CrossRef](#)]
47. Andreasen, J.G.; Larsen, U.; Knudsen, T.; Pierobon, L.; Haglind, F. Selection and optimization of pure and mixed working fluids for low grade heat utilization using organic rankine cycles. *Energy* **2014**, *73*, 204–213. [[CrossRef](#)]
48. Astolfi, M. Techno-economic Optimization of Low Temperature CSP Systems Based on ORC with Screw Expanders. *Energy Procedia* **2015**, *69*, 1100–1112. [[CrossRef](#)]
49. Dai, Y.; Wang, J.; Gao, L. Parametric optimization and comparative study of organic Rankine cycle (ORC) for low grade waste heat recovery. *Energy Convers. Manag.* **2009**, *50*, 576–582. [[CrossRef](#)]
50. Bell, I.H.; Wronski, J.; Quoilin, S.; Lemort, V. Pure and Pseudo-pure Fluid Thermophysical Property Evaluation and the Open-Source Thermophysical Property Library CoolProp. *Ind. Eng. Chem. Res.* **2014**, *53*, 2498–2508. [[CrossRef](#)]
51. Gregg, S.J.; Sing, K.S.W.; Salzberg, H.W. Adsorption Surface Area and Porosity. *J. Electrochem. Soc.* **1967**, *114*, 279C. [[CrossRef](#)]
52. Annappureddy, H.V.R.; Nune, S.K.; Motkuri, R.K.; McGrail, B.P.; Dang, L.X. A Combined Experimental and Computational Study on the Stability of Nanofluids Containing Metal Organic Frameworks. *J. Phys. Chem. B* **2015**, *119*, 8992–8999. [[CrossRef](#)]
53. Langmuir, I. The Adsorption of gases on plane surfaces of glass, mica and platinum. *J. Am. Chem. Soc.* **1918**, *40*, 1361–1403. [[CrossRef](#)]
54. Nuhnen, A.; Janiak, C. A practical guide to calculate the isosteric heat/enthalpy of adsorption: Via adsorption isotherms in metal-organic frameworks, MOFs. *Dalt. Trans.* **2020**, *49*, 10295–10307. [[CrossRef](#)]
55. Mu, B.; Walton, K.S. Thermal Analysis and Heat Capacity Study of Metal–Organic Frameworks. *J. Phys. Chem. C* **2011**, *115*, 22748–22754. [[CrossRef](#)]
56. Khanafer, K.; Vafai, K. A critical synthesis of thermophysical characteristics of nanofluids. *Int. J. Heat Mass Transf.* **2011**, *54*, 4410–4428. [[CrossRef](#)]
57. Das, S.K.; Putra, N.; Thiesen, P.; Roetzel, W. Temperature Dependence of Thermal Conductivity Enhancement for Nanofluids. *J. Heat Transf.* **2003**, *125*, 567. [[CrossRef](#)]
58. Lee, J.; Mudawar, I. Assessment of the effectiveness of nanofluids for single-phase and two-phase heat transfer in micro-channels. *Int. J. Heat Mass Transf.* **2007**, *50*, 452–463. [[CrossRef](#)]
59. Gosselin, L.; da Silva, A.K. Combined “heat transfer and power dissipation” optimization of nanofluid flows. *Appl. Phys. Lett.* **2004**, *85*, 4160–4162. [[CrossRef](#)]
60. Ardizzon, G.; Cavazzini, G.; Pavesi, G. Adaptive acceleration coefficients for a new search diversification strategy in particle swarm optimization algorithms. *Inf. Sci.* **2015**, *299*, 337–378. [[CrossRef](#)]
61. Drescher, U.; Brüggemann, D. Fluid selection for the Organic Rankine Cycle (ORC) in biomass power and heat plants. *Appl. Therm. Eng.* **2007**, *27*, 223–228. [[CrossRef](#)]
62. Alawi, O.A.; Sidik, N.A.C.; Kherbeet, A.S. Nanorefrigerant effects in heat transfer performance and energy consumption reduction: A review. *Int. Commun. Heat Mass Transf.* **2015**, *69*, 76–83. [[CrossRef](#)]
63. Mondejar, M.E.; Andreasen, J.G.; Regidor, M.; Riva, S.; Kontogeorgis, G.; Persico, G.; Haglind, F. Prospects of the use of nanofluids as working fluids for organic Rankine cycle power systems. *Energy Procedia* **2017**, *129*, 160–167. [[CrossRef](#)]